PHYSICAL REVIEW B **108**, 024409 (2023)

Damped topological magnons in honeycomb antiferromagnets

Qi-Hui Chen,[1,*] Fei-Jie Huang,[2] and Yong-Ping Fu[3]
[1] *School of Physical Science and Technology, Southwest Jiaotong University, Chengdu 610031, China*
[2] *Department of Physics, Kunming University, Kunming 650214, China*
[3] *Department of Physics, West Yunnan University, Lincang 677000, China*

(Received 3 April 2023; revised 19 June 2023; accepted 6 July 2023; published 12 July 2023)

We study magnon excitations and their interactions in honeycomb antiferromagnets with the Dzyaloshinskii-Moriya interaction. When an applied magnetic field is turned on, the classical ground state of the system is in noncollinear antiferromagnetic order. Therefore, it is crucial to consider the interactions between magnons. We find an exact and well-formed solution of the bosonic Bogoliubov–de Gennes Hamiltonian, which allows us to analytically study the topological properties and damping effects of the magnon bands. In particular, the formulas of the Berry phase and Berry curvature for the magnon bands are worked out analytically. The Mn-based trichalcogenide $MnPS_3$ is taken as a candidate material realization to estimate the order of magnitude of the thermal Hall conductivity and its evolution with the temperature and the Dzyaloshinskii-Moriya interaction strength. We develop a nonlinear spin wave theory to study the damping effects of the topological magnons and find the different damping behaviors of the upper and lower topological magnon bands when tuning the applied magnetic field. In some parameter regions, the damping effects are so strong that the free magnon description breaks down. Finally, we discuss how to observe these effects in experiments.

DOI: 10.1103/PhysRevB.108.024409

I. INTRODUCTION

The honeycomb lattice is one of the most fascinating model systems for both theoretical and experimental studies in recent decades. On the theoretical side, due to its unique single-particle dispersion spectrum, it often provides precise solutions for analyzing a variety of intriguing physics, such as the topological insulators (including Chern insulator, quantum spin Hall effect, and Weyl semimetal), topological magnons (including magnon thermal Hall effect, Dirac magnon, Weyl magnon, spin Nernst effect, and valley Hall effect), etc. [1–19]. On the experimental side, there are various materials for both electronic and magnetic systems with honeycomb structures, such as graphene, silicon, transition-metal dichalcogenides 2H-MX_2, CrX_3 (X = F, Cl, Br, I), XPS_3 (X = Mn, Fe), $CoTiO_3$, $Cr_2Ge_2Te_6$, and α-$Cu_2V_2O_7$ [20–36]. Therefore, the honeycomb lattice systems are an ideal playground for mutual verification between theoretical and experimental researches.

Magnons are the elementary excitations in the ubiquitous magnetically ordered systems. Since magnons are easily manipulated by magnetic fields and free of Joule heating, topological magnons have attracted more and more attention [37–43]. Experimentally, the thermal Hall effect was first observed in three-dimensional (3D) pyrochlore ferromagnetic insulators $Lu_2V_2O_7$, $Ho_2V_2O_7$, and $In_2Mn_2O_7$ [44,45]. Later, this effect was also reported in the two-dimensional Kagome magnet Cu(1,3-bdc) [46,47]. These advances motivate people to search for various controllable topological magnetic materials.

Early works on topological magnons focused mainly on ferromagnets described by the Heisenberg model with the Dzyaloshinskii-Moriya interaction (DMI) [3,4,37,42,48]. The ground states for these systems are collinear ferromagnetic states, where the magnons are usually well-defined quasiparticles and the interactions between magnons can be safely ignored. Therefore, the theoretical studies in this field are mainly based on the linear spin wave theory (LSWT). Recently, it was also proposed that the thermal Hall effect can be extended to antiferromagnets [38–41,49,50]. It is well known that noncollinear magnetic orders are ubiquitous in antiferromagnets, and the interactions between magnons lead to magnon decays and spectral renormalizations [51–57]. There have been some investigations on the effects of interactions on the Dirac magnons in a honeycomb lattice [6–8]. They both found that the topological properties of magnons are modulated by their interactions. The topological magnon damping effects have also been investigated in Kagome-lattice ferromagnets, where the cubic interactions of the magnons result from the unparallel relation between magnetization and DMI vector [58].

However, to the best of our knowledge, present theoretical studies on topological magnon interactions have mainly focused on ferromagnets with a honeycomb lattice. One of the main reasons is that obtaining single-particle energy spectra of noncollinear antiferromagnets generally involves diagonalizing the bosonic Bogoliubov–de Gennes (BdG) Hamiltonians. Except for some special cases [11,12], the BdG Hamiltonians are generally at least four-by-four matrices for topological antiferromagnets. It is difficult to obtain analytical eigenstates to

---

[*] qhchen@swjtu.edu.cn

further study the magnon interactions [50]. Therefore, how the magnon interactions affect the topology of antiferromagnets is still an issue of fundamental interest in topological quantum materials.

In this paper, we study the damping effects of topological magnons in honeycomb antiferromagnets with both DMI and an applied magnetic field. An elegant analytical well-formed eigenstate that allows us to investigate magnon interaction effects is found. We investigate the topological properties of the magnon bands by working out the exact Berry phase and Berry curvature. The damping effects of the topological magnons are investigated by developing a nonlinear spin wave theory. It is shown that the damping effects of upper and lower topological magnon bands have different behaviors with the tuning of the applied magnetic field. Especially in some parameter regions, the damping effects are so strong that the magnons cannot be viewed as well-defined quasiparticles.

The remainder of this paper is organized as follows. In Sec. II, we introduce the system Hamiltonian and discuss its classical phase diagram. In Sec. III, the spin wave theory is constructed. We illustrate how to diagonalize the quadratic Hamiltonian and obtain the vertex functions for the cubic Hamiltonian. The properties of the vertex function under the time-reversal transformation are also discussed. In Sec. IV, we discuss in detail the topological properties of the magnon bands and calculate the thermal Hall conductivity for $\mathrm{MnPS_3}$. In Sec. V, we calculate the damping effects of the magnon bands induced by the cubic Hamiltonian. Finally, a summary is given in Sec. VI.

II. SYSTEM HAMILTONIAN

We consider the spin Hamiltonian in the honeycomb lattice as follows:

$$H = J\sum_{\langle i,j\rangle}\mathbf{S}_i\cdot\mathbf{S}_j + \sum_{\langle\langle i,j\rangle\rangle}\mathbf{D}_{ij}\cdot\mathbf{S}_i\times\mathbf{S}_j - \sum_i \mathbf{B}\cdot\mathbf{S}_i, \tag{1}$$

where the $\mathbf{S}_i$ is the spin of magnitude S localized at $\mathbf{R}_i$ in the honeycomb lattice. The first term represents the nearest neighbor Heisenberg interaction with $J>0$ for antiferromagnets. The second term is an out-of-plane next-nearest-neighbor DMI with $\mathbf{D}_{ij}=\nu_{ij}D\hat{\mathbf{z}}$, where $\nu_{ij}=+1$ (-1) for counterclockwise (clockwise) hopping between ith and jth lattice as shown in Fig. 1(a). The last term is an applied magnetic field along the z axis with $\mathbf{B}=B\hat{\mathbf{z}}$ in unit of $g\mu_B$. To facilitate tracking the order of S in the spin wave theory, we redefine $B=hS$.

Let us discuss the mean-field ground state of the model, where the spins are viewed as classical vectors [59,60]. When the applied magnetic field is absent, the ground state is a collinear antiferromagnetic phase (CAP) assumed to be in the x direction. However, as shown in Fig. 1(b), the CAP will be instead by a noncollinear canted phase (NCP) when the applied magnetic field is turned on. The canting angle is determined by minimizing the classical ground state energy $E_{\mathrm{MF}}/(2NS)=-(3/2)J\cos 2\theta - h\sin\theta$, where N is the total number of unit cells. We obtain $\sin\theta = h/h_s$ with $h_s=6J$.

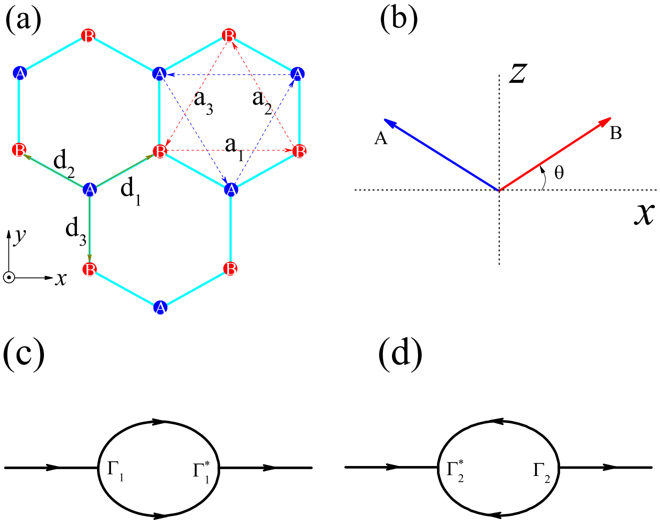

FIG. 1. (a) Schematics of a honeycomb lattice with two sublattices denoted by A and B. Three nearest-neighbor and next-nearest-neighbor vectors are labeled as $\mathbf{d}_n$ and $\mathbf{a}_n$ $(n=1,2,3)$, respectively. The dashed arrows give the positive ν_{ij} sign convention of DMI in Eq. (1). (b) The canted phase induced by the z-axis applied magnetic field, where the arrows labeled by A and B are the spins located in A and B sublattices, respectively. (c) The forward and (d) backward bubble diagrams of the magnon Green's function generated by the cubic vertices.

III. NONLINEAR SPIN WAVE THEORY

In the spin wave theory, we first need to perform a local rotation at each lattice point, so that the mean-filed directions of the spin point along the local z axis. Labeling the local frame spins as $\tilde{\mathbf{S}}_{i\alpha}$, the appropriate transformation between local and global spins is given by [50,53]

$$\begin{aligned} S^x_{i,A(B)} &= \pm\tilde{S}^x_{i,A(B)}\sin\theta \pm \tilde{S}^z_{i,A(B)}\cos\theta,\\ S^y_{i,A(B)} &= \pm\tilde{S}^y_{i,A(B)},\\ S^z_{i,A(B)} &= -\tilde{S}^x_{i,A(B)}\cos\theta + \tilde{S}^z_{i,A(B)}\sin\theta, \end{aligned} \tag{2}$$

where ± correspond to sublattices A and B, respectively.

With the rotation, the Hamiltonian Eq. (1) can be rewritten in the local reference frames as $H=H_J+H_D+H_h$ with

$$\begin{aligned} H_J &= J\sum_{\langle ij\rangle}\big[\cos 2\theta\big(\tilde{S}^x_i\tilde{S}^x_j - \tilde{S}^z_i\tilde{S}^z_j\big) - \tilde{S}^y_i\tilde{S}^y_j \\ &\quad - \sin 2\theta\big(\tilde{S}^x_i\tilde{S}^z_j + \tilde{S}^z_i\tilde{S}^x_j\big)\big],\\ H_D &= D\sum_{\langle\langle ij\rangle\rangle}\sin\theta\big(\tilde{S}^x_i\tilde{S}^y_j - \tilde{S}^y_i\tilde{S}^x_j\big)\\ &\quad + \cos\theta\big(\tilde{S}^z_i\tilde{S}^y_j - \tilde{S}^y_i\tilde{S}^z_j\big),\\ H_h &= hS\sum_i\big(\cos\theta\tilde{S}^x_i - \sin\theta\tilde{S}^z_i\big). \end{aligned} \tag{3}$$

Let us discuss two collinear phases. The first one is the fully polarized phase (FPP) with $\theta=\pi/2$. In this case the third term in H_J and the second term in H_D will disappear. According to the spin wave theory, these terms will lead to the magnon cubic interactions. Therefore, the magnons are not affected by the cubic interactions in this case. The second one is the CAP with $\theta = 0$ when the applied magnetic field is absent. In this case the third term in H_J and the first term in H_D will disappear. At this point, if we still use the linear spin wave approximation, we will find that H_D does not affect the physics of the system. However, there will be the spin Nernst effect caused by H_D, which can be confirmed by an appropriate spin transformation [11,12,50]. In other words, to capture the real physics, the staggered Néel order should point in the z-axis direction at zero magnetic field.

Then, we perform a standard Holstein-Primakoff (HP) transformation to the local spin operators $\tilde{\mathbf{S}}_i$ in Eq. (3),

$$\begin{aligned}\tilde{\mathbf{S}}_i^x &= \frac{1}{2}\left(\sqrt{2S - a_i^\dagger a_i}\,a_i^\dagger + a_i\sqrt{2S - a_i^\dagger a_i}\right),\\ \tilde{\mathbf{S}}_i^y &= \frac{i}{2}\left(\sqrt{2S - a_i^\dagger a_i}\,a_i^\dagger - a_i\sqrt{2S - a_i^\dagger a_i}\right),\\ \tilde{\mathbf{S}}_i^z &= S - a_i^\dagger a_i,\end{aligned} \tag{4}$$

where $a_i^\dagger$ (a_i) are bosonic creation (annihilation) operators. In the large-S limit, to capture the lowest order interaction effects of magnons, we expand the square root parts of Eq. (4) up to the order of $a_i^\dagger a_i/\sqrt{S}$, i.e.,

$$\sqrt{2S - a_i^\dagger a_i} \approx \sqrt{2S} - \frac{\sqrt{2}}{4}\frac{a_i^\dagger a_i}{\sqrt{S}}. \tag{5}$$

Then, substituting Eqs. (4) and (5) into Eq. (3), up to cubic terms of $a_i^\dagger$ (a_i), the expanded Hamiltonian is obtained as

$$H = H^{(0)} + H^{(1)} + H^{(2)} + H^{(3)} + \cdots, \tag{6}$$

where $H^{(n)}$ (with $n = 0, 1, 2, 3$) gives the $S^{2-n/2}$th-order contribution. The first term $H^{(0)} = 2NS^2E_{\mathrm{MF}}$ is the classical ground state energy. The second term $H^{(1)}$ vanishes due to the energy minimum. The magnon energy bands are obtained by diagonalizing the quadratic Hamiltonian $H^{(2)}$. The magnon damping effects originate from the cubic Hamiltonian $H^{(3)}$. In this paper, we will not discuss the effects of higher-order interactions. The specific forms of $H^{(2)}$ and $H^{(3)}$ are given in the following two subsections.

A. Quadratic Hamiltonian

By performing the Fourier transformation, the quadratic Hamiltonian $H^{(2)}$ is written in momentum space as

$$\begin{aligned}H^{(2)} = 3JS\sum_{\mathbf k}[&(1+\mathcal{D}_{\mathbf k})a_{1\mathbf k}^\dagger a_{1\mathbf k} + (1-\mathcal{D}_{\mathbf k})a_{2\mathbf k}^\dagger a_{2\mathbf k}\\ &- (s_\theta f_{\mathbf k} a_{1\mathbf k}^\dagger a_{2\mathbf k} - (1-s_\theta)f_{\mathbf k} a_{1\mathbf k}^\dagger a_{2-\mathbf k}^\dagger + \mathrm{H.c.})],\end{aligned} \tag{7}$$

where $a_{1(2)}^\dagger$ denotes the operator on the sublattice A (B), and $\mathcal{D}_{\mathbf k} = (D/J)\sqrt{s_\theta}g_{\mathbf k}$ with $s_\theta = \sin^2\theta$. $\mathcal{D}_{\mathbf k}$ is an odd function of $\mathbf{k}$ due to $g_{\mathbf k} = (2/3)\sum_n \sin(\mathbf{k}\cdot\mathbf{a}_n)$ where $\mathbf{a}_n$ are the vectors linking next nearest neighbors shown in Fig. 1(a). $f_{\mathbf k} = (1/3)\sum_n \exp(i\mathbf{k}\cdot\mathbf{d}_n) = |f_{\mathbf k}|\exp(i\varphi_{\mathbf k})$ is the complex nearest-neighbor hopping amplitude with $|f_{\mathbf k}| = |f_{-\mathbf k}|$ and $\varphi_{\mathbf k} = -\varphi_{-\mathbf k}$.

For $D = 0$, the method of diagonalization of $H^{(2)}$ has been discussed by Maksimov *et al.* [53]. The conditions of applying this method are given by Chernyshev [54,55]. Although the Hamiltonian in Eq. (7) does not satisfy those conditions, a similar procedure is still applicable.

First, we use a unitary transformation $a_{\alpha\mathbf k}^\dagger = e^{i(-1)^\alpha\varphi_{\mathbf k}/2}\sum_\mu T_{\mathbf k}^{\alpha\mu}c_{\mu\mathbf k}^\dagger$ to transform the field operators $(a, a^\dagger)$ to $(c, c^\dagger)$, where $T_{\mathbf k}$ is a real matrix:

$$T_{\mathbf k} = \begin{bmatrix}-\cos\psi_{\mathbf k} & \sin\psi_{\mathbf k}\\ \sin\psi_{\mathbf k} & \cos\psi_{\mathbf k}\end{bmatrix}. \tag{8}$$

Surprisingly, we can figure out the elements of $T_{\mathbf k}$ as $\cos\psi_{\mathbf k} = \sqrt{(\eta_{\mathbf k} + \mathcal{D}_{\mathbf k})/2\eta_{\mathbf k}}$ and $\sin\psi_{\mathbf k} = \sqrt{(\eta_{\mathbf k} - \mathcal{D}_{\mathbf k})/2\eta_{\mathbf k}}$, with $\eta_{\mathbf k} = \sqrt{\mathcal{D}_{\mathbf k}^2 + s_\theta^2|f_{\mathbf k}|^2}$. Because $\eta_{\mathbf k}$ is an even function of $\mathbf{k}$, we have $\cos\psi_{-\mathbf k} = \sin\psi_{\mathbf k}$. After this transformation, $H^{(2)}$ can be rewritten in terms of the field operators $(c,\ c^\dagger)$ as

$$H^{(2)} = 3JS\sum_{\mathbf k,\mu}\left[A_{\mu\mathbf k}c_{\mu\mathbf k}^\dagger c_{\mu\mathbf k} - \frac{B_{\mu\mathbf k}}{2}(c_{\mu\mathbf k}c_{\mu-\mathbf k} + \mathrm{H.c.})\right], \tag{9}$$

where the two real functions are $A_{\mu\mathbf k} = 1 - (-1)^\mu\eta_{\mathbf k}$ and $B_{\mu\mathbf k} = (-1)^\mu(s_\theta - 1)|f_{\mathbf k}|$.

Then, $H^{(2)}$ in Eq. (9) can be diagonalized by the standard Bogoliubov transformation $c_{\mu\mathbf k} = u_{\mu\mathbf k}b_{\mu\mathbf k} + v_{\mu\mathbf k}b_{\mu-\mathbf k}^\dagger$ [also written as $c_{\mu\mathbf k} = \cosh(\chi_{\mu\mathbf k})b_{\mu\mathbf k} + \sinh(\chi_{\mu\mathbf k})b_{\mu-\mathbf k}^\dagger$] with $2u_{\mu\mathbf k}v_{\mu\mathbf k} = B_{\mu\mathbf k}/\omega_{\mu\mathbf k}$, $u_{\mu\mathbf k}^2 + v_{\mu\mathbf k}^2 = A_{\mu\mathbf k}/\omega_{\mu\mathbf k}$ and $\omega_{\mu\mathbf k} = \sqrt{A_{\mu\mathbf k}^2 - B_{\mu\mathbf k}^2}$. An explicit expression for these quantities is given in Appendix A. The two magnon bands are given by

$$E_{\pm,\mathbf k} = 3JS\sqrt{(1\pm\eta_{\mathbf k})^2 - (s_\theta - 1)^2|f_{\mathbf k}|^2}, \tag{10}$$

where + and − correspond to the upper and lower magnon bands, respectively. The magnon bands with different s_θ are shown in Fig. 4. In the FPP, $E_{\pm,\mathbf k}$ are reduced to be $\mathcal{E}_{\pm,\mathbf k} = 3JS(1\pm\eta_{\mathbf k})$. And for the CAP, $E_{\pm,\mathbf k} = 3JS\sqrt{1 - |f_{\mathbf k}|^2}$ are degenerate. Note that the energy gaps at K (K') are $\Delta_K = 6DS\sqrt{3s_\theta}$, which is independent of J and can be used to extract the strength of DMI in the experiments.

B. Cubic Hamiltonian

The cubic Hamiltonian $H^{(3)}$ in momentum space reads

$$H^{(3)} = \sum_{\mathbf k,\mathbf q}\sum_{\alpha\beta}\left(V_{\mathbf q}^{\alpha\beta}a_{\beta\mathbf q}^\dagger a_{\alpha\mathbf k}^\dagger a_{\alpha-\mathbf p} + \mathrm{H.c.}\right), \tag{11}$$

where $-\mathbf{p} = \mathbf{k} + \mathbf{q}$ and the interacting vertices are given by the elements of the vertex matrix $V_{\mathbf q}$ as

$$V_{\mathbf q} = 3\sqrt{\frac{S}{2N}}\begin{bmatrix}-D\cos\theta g_{\mathbf q} & J\sin(2\theta)f_{\mathbf q}^*\\ J\sin(2\theta)f_{\mathbf q} & D\cos\theta g_{\mathbf q}\end{bmatrix}. \tag{12}$$

It is worth noting that, due to the DMI, $V_{\mathbf q}$ does not have the time-reversal symmetry, i.e., $V_{-\mathbf q} \neq (V_{\mathbf q})^*$. By sequentially performing the unitary and Bogoliubov transformations, we can write out the cubic Hamiltonian in terms of field operators $(b, b^\dagger)$ as

$$\begin{aligned}H^{(3)} = \sum_{\mathbf k,\mathbf q}\sum_{\rho\nu\mu}\bigg(&\frac{1}{2!}\Gamma_{1,\mathbf{kqp}}^{\rho\nu\mu}b_{\rho\mathbf q}^\dagger b_{\nu\mathbf k}^\dagger b_{\mu-\mathbf p}\\ &+ \frac{1}{3!}\Gamma_{2,\mathbf{kqp}}^{\rho\nu\mu}b_{\rho\mathbf q}^\dagger b_{\nu\mathbf k}^\dagger b_{\mu\mathbf p}^\dagger + \mathrm{H.c.}\bigg).\end{aligned} \tag{13}$$

It has the same form as the one obtained by Maksimov *et al.* [53]; however, the interaction vertices are very different. Since the DMI breaks the time-reversal symmetry, both the decay vertices $\Gamma^{\rho\nu\mu}_{1,\mathbf{qkp}}$ and the source vertices $\Gamma^{\rho\nu\mu}_{2,\mathbf{qkp}}$ can be divided into two parts: $\Gamma^{\rho\nu\mu}_{\alpha,\mathbf{qkp}} = \Gamma^{\rho\nu\mu}_{\alpha S,\mathbf{qkp}} + \Gamma^{\rho\nu\mu}_{\alpha A,\mathbf{qkp}}$, where $\Gamma^{\rho\nu\mu}_{\alpha S,\mathbf{qkp}}$ conserve the time-reversal symmetry $\Gamma^{\rho\nu\mu}_{\alpha S,-(\mathbf{qkp})} = (\Gamma^{\rho\nu\mu}_{\alpha S,\mathbf{qkp}})^*$, while $\Gamma^{\rho\nu\mu}_{\alpha A,\mathbf{qkp}}$ have the time-reversal antisymmetry $\Gamma^{\rho\nu\mu}_{\alpha A,-(\mathbf{qkp})} = -(\Gamma^{\rho\nu\mu}_{\alpha A,\mathbf{qkp}})^*$. Because of the presence of the source vertices, it is obvious that the cubic Hamiltonian is also different from that obtained in a ferromagnet [8]. The explicit forms of $\Gamma^{\rho\nu\mu}_{\alpha,\mathbf{qkp}}$ are given in Appendix B.

Compared with the situation where the DMI is absent [53], we can see that the impacts induced by the DMI are twofold. First, the DMI strongly modifies the energy spectrum of the magnon at K (K'), leading to the opening of energy gaps at the Dirac points. Furthermore, as we will see in the next section, this leads to topologically nontrivial magnon bands. Second, the DMI causes the time-reversal antisymmetric part $\Gamma^{\rho\nu\mu}_{\alpha A,\mathbf{qkp}}$ which appears in the decay and source vertices of the cubic Hamiltonian. A natural question is whether $\Gamma^{\rho\nu\mu}_{\alpha A,\mathbf{qkp}}$ causes the change of some physical quantities (such as the decay rates and the self-energies discussed in the following section) under the time-reversal operation, i.e., $\mathcal{X}(\mathbf{k}) \neq \mathcal{X}(-\mathbf{k})$ for physical quantity $\mathcal{X}$.

To answer the question, we need to consider $|\Gamma^{\rho\nu\mu}_{\alpha,\mathbf{qkp}}|^2$ which appears in the sums of the $1/S$ order of the perturbative expansion. According to the above definitions, we have $|\Gamma^{\rho\nu\mu}_{\alpha,\mathbf{qkp}}|^2 = |\Gamma^{\rho\nu\mu}_{\alpha S,\mathbf{qkp}}|^2 + |\Gamma^{\rho\nu\mu}_{\alpha A,\mathbf{qkp}}|^2 + 2\,\mathrm{Re}[\Gamma^{\rho\nu\mu}_{\alpha S,\mathbf{qkp}}(\Gamma^{\rho\nu\mu}_{\alpha A,\mathbf{qkp}})^*]$, where the last term of the right-hand side changes its sign under the time-reversal transformation. Using the definitions of $\Gamma^{\rho\nu\mu}_{\alpha S,\mathbf{qkp}}$ and $\Gamma^{\rho\nu\mu}_{\alpha A,\mathbf{qkp}}$ in Appendix B, after some tedious calculations, we find out that $\Gamma^{\rho\nu\mu}_{\alpha A,\mathbf{qkp}}$ is real while $\Gamma^{\rho\nu\mu}_{\alpha S,\mathbf{qkp}}$ is imaginary if $\rho + \nu + \mu$ is odd, or vice versa if $\rho + \nu + \mu$ is even. Then, we have $\mathrm{Re}[\Gamma^{\rho\nu\mu}_{\alpha S,\mathbf{qkp}}(\Gamma^{\rho\nu\mu}_{\alpha A,\mathbf{qkp}})^*] = 0$, as $\Gamma^{\rho\nu\mu}_{\alpha S,\mathbf{qkp}}(\Gamma^{\rho\nu\mu}_{\alpha A,\mathbf{qkp}})^*$ has no real part. Hence, $|\Gamma^{\rho\nu\mu}_{\alpha,\mathbf{qkp}}|^2$ is invariant under the time-reversal transformation. We conclude that, up to the $1/S$ order, the physical quantities which are functions of $|\Gamma^{\rho\nu\mu}_{\alpha,\mathbf{qkp}}|^2$ and magnon spectra $E_{\pm,\mathbf{k}}$ are invariant under time-reversal transformation, like the decay rates given in the Sec. V.

On the other hand, it is easy to verify that the symmetry part $\Gamma^{\rho\nu\mu}_{\alpha S,\mathbf{qkp}}$ is dominant near the momentum Γ point, while the antisymmetry part $\Gamma^{\rho\nu\mu}_{\alpha A,\mathbf{qkp}}$ is dominant near the K (K') points. Therefore, we find that the decays of lower magnon bands are almost not affected by DMI (or equivalently by $\Gamma^{\rho\nu\mu}_{\alpha A,\mathbf{qkp}}$) near the Γ point. We can also expect that the physical quantities related to $\Gamma^{\rho\nu\mu}_{\alpha A,\mathbf{qkp}}$ around the K (K') point will be greatly affected by $\Gamma^{\rho\nu\mu}_{\alpha A,\mathbf{qkp}}$.

IV. TOPOLOGY OF THE MAGNON BANDS AND THERMAL HALL CONDUCTIVITY

Berry curvature $\Omega_\alpha(\mathbf{k})$ is an important physical quantity to describe the topological properties of the αth energy band. According to the diagonalization procedures of $H^{(2)}$, we can explicitly write down the eigenvectors $|\Psi_\pm(\mathbf{k})\rangle$ which are given in Appendix A. The Berry curvatures are calculated by $\Omega_\pm(\mathbf{k}) = [-\mathrm{Im}\{\langle\nabla\Psi_\pm(\mathbf{k})| \times \Lambda|\nabla\Psi_\pm(\mathbf{k})\rangle\}]_z$, where $\Lambda = \mathrm{diag}(1, 1, -1, -1)$ is a diagonal matrix and $[\cdot]_z$ means taking the z component. We find that the analytical expressions of the Berry curvature can be divided into two parts which are given by

$$\Omega_\pm(\mathbf{k}) = \Omega_{\pm,\psi}(\mathbf{k}) + \Omega_{\pm,\chi}(\mathbf{k}) \tag{14}$$

with

$$\begin{aligned}\Omega_{\pm,\psi}(\mathbf{k}) &= (\mp \sin 2\psi_\mathbf{k} \cosh 2\chi_{\pm,\mathbf{k}})\nabla\varphi_\mathbf{k} \times \nabla\psi_\mathbf{k},\\ \Omega_{\pm,\chi}(\mathbf{k}) &= (\pm \sinh 2\chi_{\pm,\mathbf{k}} \cos 2\psi_\mathbf{k})\nabla\varphi_\mathbf{k} \times \nabla\chi_{\pm,\mathbf{k}},\end{aligned} \tag{15}$$

where $\chi_{1(2)\mathbf{k}}$ are denoted by $\chi_{+(-),\mathbf{k}}$, respectively. The topology of the magnon bands is characterized by the Chern numbers $C_\pm$, which are defined as the integration of the corresponding Berry curvature over the Brillouin zone (BZ). The Chern numbers contributed by $\Omega_{\pm,\psi}$ and $\Omega_{\pm,\chi}$ are

$$\begin{aligned}C_{\pm,\psi} &= \frac{1}{2\pi}\int_{BZ} \Omega_{\pm,\psi}(\mathbf{k})dk_x dk_y,\\ C_{\pm,\chi} &= \frac{1}{2\pi}\int_{BZ} \Omega_{\pm,\chi}(\mathbf{k})dk_x dk_y.\end{aligned} \tag{16}$$

The Chern numbers are given by $C_\pm = C_{\pm,\psi} + C_{\pm,\chi}$.

In the FPP, because $\cosh\chi_{\pm,\mathbf{k}} = 1$ and $\nabla\chi_{\pm,\mathbf{k}} = 0$, we have $C_{\pm,\chi} = 0$. Then, the Chern numbers are reduced to $C_\pm = C_{\pm,\psi} = \mp(1/4\pi)\int_\mathcal{S} \sin(2\psi)d(2\psi)d\varphi$ which give the area on the unit sphere $\mathcal{S}$ if we view 2ψ, φ as the polar and azimuth angles, respectively. Because the BZ over which we integrated the Berry curvature is a closed and orientable manifold (torus), the integral must be an integer. By numerical calculation, we obtain the Chern numbers as -1 and $+1$ for the upper and lower bands, respectively. In the NCP, both the $C_{\pm,\psi}$ and $C_{\pm,\chi}$ are not integers. However, according to the gauge field theory [61], the integral of their sum remains an integer as shown in Fig. 2(a).

With the help of the exact eigenvectors $|\Psi_\pm(\mathbf{k})\rangle$, we can also prove analytically that the Chern numbers are integers. For antiferromagnets, the Berry vector potentials of the magnon energy bands are defined as

$$\mathbf{A}_\pm(\mathbf{k}) = i\langle\Psi_\pm(\mathbf{k})|\Lambda|\nabla\Psi_\pm(\mathbf{k})\rangle, \tag{17}$$

which are two-dimensional vectors in the $\mathbf{k}$ plane. It is obvious that the Berry curvature can also be calculated by $\Omega_\pm(\mathbf{k}) = [\nabla \times \mathbf{A}_\pm(\mathbf{k})]_z$. According to Stokes's theorem, the integral of the Berry curvature over BZ must be zero if $\mathbf{A}_\pm(\mathbf{k})$ is nonsingular on the whole BZ. Through a direct calculation, we obtain

$$\mathbf{A}_\pm(\mathbf{k}) = \mp\cosh 2\chi_{\pm,\mathbf{k}} \cos 2\psi_\mathbf{k} \nabla\varphi_\mathbf{k}. \tag{18}$$

It can be confirmed that K and K' are singular points of $\mathbf{A}_\pm(\mathbf{k})$. We take the upper band as an example to demonstrate the singularity of $\mathbf{A}_+(\mathbf{k})$ at K (K'), which is shown in Fig. 2(b).

As shown in Fig. 2(c), because $\mathbf{A}_+(\mathbf{k})$ has no singularity in the cyan region of the BZ, according to Stokes's theorem, the integral of Berry curvature in this region can be transformed

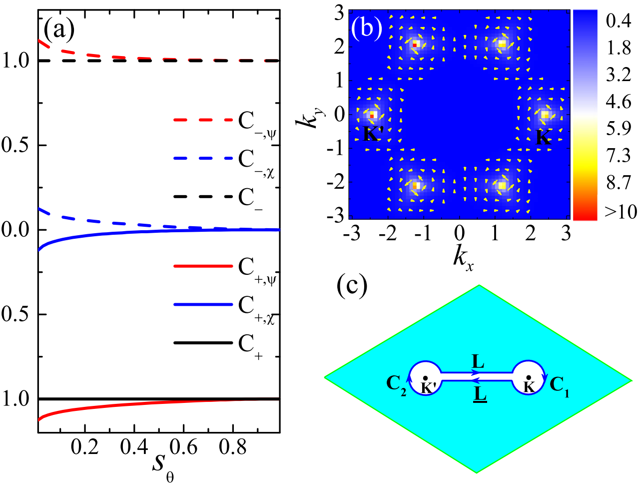

FIG. 2. (a) The Chern numbers $C_\pm$ and their contributions from $C_{\pm,\psi}$ and $C_{\pm,\chi}$ are plotted with $D = 0.1J$ and different values of s_θ. (b) The Berry vector potential $\mathbf{A}_+(\mathbf{k})$ is shown by a vector field plot, with the color plot indicating its magnitude $|\mathbf{A}_+(\mathbf{k})|$, where $s_\theta = 0.9$ and $D = 0.1J$. (c) The Brillouin zone which is spanned by two primitive vectors of the reciprocal lattice is equivalent to the surface of a torus due to the periodic boundary conditions. The cyan area is surrounded by a blue line with arrows pointing in the positive direction.

into a line integral of its boundary (blue line). Taking the limit conditions, L to coincides with $\underline{L}$, and the radii of circles C_1 and C_2 tend toward zero, $r \to 0$, then the integrals of $\mathbf{A}_+(\mathbf{k})$ over L and $\underline{L}$ cancel out, hence

$$\int_{BZ} \Omega_+(\mathbf{k}) dS = \lim_{r\to 0} \oint_{C_1+C_2} \mathbf{A}_+(\mathbf{k}) d\mathbf{l}. \tag{19}$$

By expanding $\mathbf{A}_+(\mathbf{k})$ around K and K' respectively, the integral on the right side of Eq. (19) gives -2π. Therefore, the Chern number C_+ of the upper band is -1. The same discussions can also be used for the lower band.

The thermal Hall conductivity is related to the Berry curvatures by

$$\kappa_{xy} = -\frac{k_B^2 T}{\hbar V}\sum_{\mathbf{k}}\sum_{\alpha=1}^{M}\left\{c_2(g(\epsilon_{n,\mathbf{k}})) - \frac{\pi^2}{3}\right\}\Omega_{\alpha\mathbf{k}}, \tag{20}$$

where $g(\epsilon_{n,\mathbf{k}}) = [e^{\epsilon_{n,\mathbf{k}}/k_B T} - 1]^{-1}$ is the bosonic distribution function, $c_2(x) = (1+x)(\ln\frac{1+x}{x})^2 - (\ln x)^2 - 2\,\mathrm{Li}_2(-x)$, $\mathrm{Li}_2(x)$ is the dilogarithm [40], and M is the number of sublattices. In experiments, MnPS$_3$ can be considered a two-dimensional Heisenberg antiferromagnet in which Mn^{2+} ions with $S = 5/2$ are arranged in a honeycomb lattice [62,63]. An out-of-plane DMI is also allowed due to the lack of an inversion center at the midpoint between the next-nearest-neighbor sites.

We take MnPS$_3$ as a candidate material realization to estimate the order of magnitude of the thermal Hall conductivity, and show the evolution of the thermal Hall conductivity with the temperature and the DMI strength. The structure of MnPS$_3$ is monoclinic, with the $C2/m$ space group. The unit cell parameters are $a = 6.077$ Å, $b = 10.524$ Å, $c = 6.769$ Å, and $\beta = 107.35°$, and the nearest-neighbor exchange interactions are $J = 0.77$ meV. We ignored the second- and the third-nearest-neighbor exchange couplings because they conserve the symmetry of the system Hamiltonian Eq. (1) and thus do not qualitatively change the main physics discussed here.

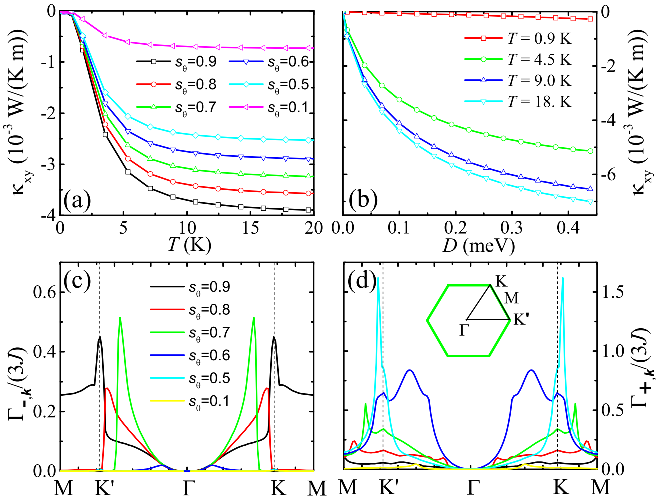

FIG. 3. The thermal Hall conductivities of MnPS$_3$ as a function of temperature (T) and DMI strength (D) are given in (a) and (b), respectively. We have chosen $D = 0.077$ meV and $s_\theta = 0.9$ in panels (a) and (b), respectively. Panels (c) and (d) are the magnon decay rates $\Gamma_{\mu,\mathbf{k}}$ for lower and upper bands, respectively. The decay rates for different values of s_θ are plotted with different colors. The inset in (d) sketches the first Brillouin zone of the honeycomb lattice.

The thermal Hall conductivities κ_{xy} as a function of temperature and DMI strength are shown in Figs. 3(a) and 3(b), respectively. We can see that as long as s_θ and D are not too small, the Hall thermal conductivity reaches the order of 10^{-3} W/K m, which is exactly the range that can be measured experimentally [44]. In the limit of $s_\theta \to 0$, it can be proved that $\kappa_{xy} \to 0$ due to $\mathcal{D}_\mathbf{k} \to 0$ in Eq. (7). This means that the thermal Hall effect is absent when the applied magnetic field is turned off, which is consistent with the Ref. [50]. However, it can be expected that the spin Nernst effect will occur at this time [12]. Finally, as shown in Figs. 3(a) and 3(b), the thermal Hall conductivities increase monotonically with the increase in temperature and DMI strength. It is worth noting that D should be less than the critical value for the spin texture formation.

V. MAGNON DAMPLING INDUCED BY INTERACTION

One important feature of the interactions between magnons is the damping effects which will lead to a finite lifetime for the magnons. The damping effect determines many basic properties of a quantum many-body system, such as transport, thermalization, etc. We invoke the standard diagrammatic technique for bosons at zero temperature to investigate the damping effect induced by $H^{(3)}$. Up to order $1/S$, the one-magnon Green's function is contributed by the "forward" and "backward bubble" diagrams shown in Figs. 1(c) and 1(d), respectively. From those two diagrams, the normal self-energies are extracted as

$$\Sigma^{\alpha\beta}_{F,\mathbf{k}} = \frac{1}{2}\sum_{\mathbf{q}}\sum_{\nu\nu'} \frac{\Gamma^{\nu\nu'\beta}_{1,\mathbf{q}(\mathbf{k}-\mathbf{q})(-\mathbf{k})}\left(\Gamma^{\nu\nu'\alpha}_{1,\mathbf{q}(\mathbf{k}-\mathbf{q})(-\mathbf{k})}\right)^*}{\omega - E_{\nu,\mathbf{q}} - E_{\nu',\mathbf{k}-\mathbf{q}} + i\,0^+}, \tag{21}$$

$$\Sigma^{\alpha\beta}_{B,\mathbf{k}} = -\frac{1}{2}\sum_{\mathbf{q}}\sum_{\nu\nu'} \frac{\Gamma^{\alpha\nu\nu'}_{2,\mathbf{kq}(-\mathbf{k}-\mathbf{q})}\left(\Gamma^{\beta\nu\nu'}_{2,\mathbf{kq}(-\mathbf{k}-\mathbf{q})}\right)^*}{\omega + E_{\nu,\mathbf{q}} + E_{\nu',\mathbf{k}+\mathbf{q}} - i\,0^+}. \tag{22}$$

Note that although Eqs. (21) and (22) give the self-energy matrices, we only need to consider their diagonal elements for the correction of order $1/S$. For the same reason, we ignored the contributions of anomalous self-energies.

The damping effect of magnons originates from the imaginary part of the self-energy. In this study, the imaginary part of the self-energy comes from the contribution of Eq. (21). In the lowest Born approximation [51,58], the decay rate can be expressed as

$$\Gamma_{\mu,\mathbf{k}} = \frac{\pi}{2}\sum_{\mathbf{q},\nu\nu'}\left|\Gamma^{\nu\nu'\mu}_{1,\mathbf{q}(\mathbf{k}-\mathbf{q})(-\mathbf{k})}\right|^2 \delta(E_{\mu,\mathbf{k}} - E_{\nu,\mathbf{q}} - E_{\nu',\mathbf{k}-\mathbf{q}}). \tag{23}$$

We note that in the Born approximation, decays are only allowed if kinematic conditions $E_{\mu,\mathbf{k}} = E_{\nu,\mathbf{q}} + E_{\nu',\mathbf{k}-\mathbf{q}}$ are satisfied. In other words, decays are only possible when the single-magnon spectrum overlaps the two-magnon continuum. The momentum-resolved two-magnon density of states (DOS) is defined as [8]

$$D_{\mathbf{k}}(\omega) = \frac{1}{N}\sum_{\mathbf{q},\nu\nu'} \delta(\omega - E_{\nu,\mathbf{q}} - E_{\nu',\mathbf{k}-\mathbf{q}}), \tag{24}$$

which is a useful quantitative characteristic of the two-magnon continuum. We show the two-magnon DOS with the color plot in Fig. 4.

The evolutions of the decay rate $\Gamma_{\mu,\mathbf{k}}$ of the upper and lower magnon bands with s_θ are shown in Fig. 3. In the summation of Eq. (23), we have used a system with $2 \times 2000 \times 2000$ points: a sparse mesh for the momentum $\mathbf{k}$ of 4×10^6 points in the whole BZ. An artificial broadening of the δ function $0^+ = 3 \times 10^{-4}J$ was also used. To clearly show the influence of decay rates on topological magnons, we also draw the decay rates on the magnon bands in Fig. 4. As expected, in Fig. 4 the decay only occurs when the single-magnon spectrums intersect with the two-magnon continuum.

It can be seen from those figures that the magnon decay rates depend on (i) the strength of the interaction of $H^{(3)}$ and (ii) the intersection positions of the single-magnon spectrum and the two-magnon continuum. First, in the FPP, the topological magnons do not suffer decay from $H^{(3)}$ since $V_{\mathbf{q}} = 0$ in Eq. (12). Second, as shown in Fig. 4(f), when the system tends to the CAP, although the interaction strength of $H^{(3)}$ is very strong, the decay rates are still weak; this is because the single-magnon bands are far away from the region where the two-magnon continuum is strong. Third, as discussed by Maksimov *et al.* [53], there is a critical $s_{\theta,c} = 0.6$ for the long-wavelength part of the lower band, and the decays will occur only when $s_\theta > s_{\theta,c}$. Fourth, for the long-wavelength part of the upper band, as shown in Figs. 4(a) and 4(b), there is also a decay-free region when $\sim 0.7 < s_\theta < 1$. In general, the decay of magnons at long wavelengths is relatively weak in both the upper and lower bands.

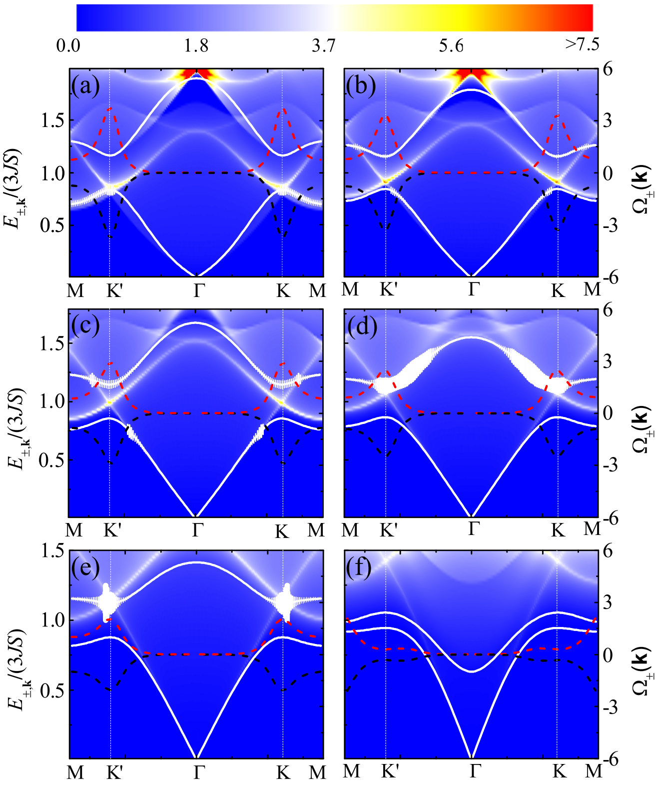

FIG. 4. Magnon bands are represented by white lines with vertical bars whose lengths are proportional to its decay rates shown in Fig. 3. Berry curvatures for upper and lower bands are plotted by black and red dashed lines, respectively. The color plots give the two-magnon DOS in Eq. (24). Blue (red) color indicates zero (maximal) two-magnon DOS. The parameters are $D = 0.1J$ and $s_\theta = 0.9, 0.8, 0.7, 0.6, 0.5, 0.1$ for (a)–(f), respectively.

Finally, we are very interested in the decays of magnons near K (K'). Because the nonzero Berry curvatures are mainly concentrated in this region, the magnons near K (K') will be responsible for the thermal (or spin) Hall effect. We know that magnons can be considered as well-defined and independent quasiparticles only if they have sufficiently long lifetimes, which are given by $\tau_{\mu,\mathbf{k}} = \hbar\Gamma^{-1}_{\mu,\mathbf{k}}$. Or, equivalently, the condition $\Gamma_{\mu,\mathbf{k}} \ll E_{\mu,\mathbf{k}}$ is required. We find that the decay rates of the upper and lower magnon bands show different behaviors as s_θ decreases. In some parameter regions, the quasiparticle picture breaks down where the quasiparticle condition is not satisfied. For example, the decays of the upper band in Fig. 4(a) are very weak, while the decays of the lower band along K-M are very strong. In Fig. 4(d), there are strong decays in the upper band and almost no decay in the lower band. In Fig. 4(e), the decay near K (K') in the upper band is very strong, even $\Gamma_{\mu,\mathbf{k}} > E_{\mu,\mathbf{k}}$ in some momentums, while the lower band has no decay at all. From these examples, in general, we conclude that strong decays should occur when the single-magnon spectrum intersects with the maximum of the two-magnon continuum.

VI. SUMMARY

In summary, we have investigated the magnon excitations in honeycomb antiferromagnets with DMI and an applied magnetic field. We find an analytical solution which allows us to analytically study the topological properties and the damping effect of the magnon bands. In particular, we work out the analytical formulas of the Berry phase and Berry curvature for the energy bands. By both numerical and analytical methods, we also show that the Chern numbers for the upper and lower magnon bands are exactly ∓1, respectively. By the nonlinear spin wave theory, we further study the damping effect of the topological magnons in the NCP. We find that the damping behaviors of the upper and lower magnon bands are different with the variation of the magnetic field. This means that the magnetic field can be used to manipulate the transport properties of the system.

In experiments, the Mn-based trichalcogenide $\mathrm{MnPS_3}$ [29] may be viewed as a potential candidate to confirm our results. Using the experimental parameters of this material, we have shown the thermal Hall conductivity as a function of temperature and strength of DMI. We found that thermal Hall conductivities are of the order of magnitude that can be detected in an experiment. The topological properties of the magnon bands in $\mathrm{MnPS_3}$ can be confirmed by a transverse magnon Hall current induced by an in-plane temperature gradient. One important manifestation of the magnon damping effect is the broadening of the magnon spectrum in experiments. To the best of our knowledge, how the damping effect affects the magnon Hall current of the system is still an open question both in theoretical and experimental studies. We believe the results here will provide an ideal platform for future studies.

ACKNOWLEDGMENT

This work is supported by the National Natural Science foundation of China under Grant No. 12175185.

APPENDIX A: THE DIAGONALIZATION OF QUADRATIC HAMILTONIAN $H^{(2)}$

In the main text, we discussed how to diagonalize $H^{(2)}$ by the field operator transformation; now we give the matrix method to diagonalize $H^{(2)}$. For this purpose, we rewrite $H^{(2)}$ as

$$H^{(2)} = \frac{3JS}{2}\sum_{\mathbf{k}}(\phi^\dagger(\mathbf{k}), \tilde{\phi}(-\mathbf{k}))\mathcal{H}(\mathbf{k})\begin{pmatrix}\phi(\mathbf{k})\\ \tilde{\phi}^\dagger(-\mathbf{k})\end{pmatrix}, \tag{A1}$$

where a constant term has been neglected, $\phi^\dagger(\mathbf{k}) = (a^\dagger_{1\mathbf{k}}, a^\dagger_{2\mathbf{k}})$, and the tilde on the top of ϕ means the transpose operation. The bosonic Bogoliubov Hamiltonian $\mathcal{H}(\mathbf{k})$ has the following form:

$$\mathcal{H}(\mathbf{k}) = \begin{bmatrix}\mathcal{A}(\mathbf{k}) & \mathcal{B}(\mathbf{k})\\ \mathcal{B}^*(-\mathbf{k}) & \mathcal{A}^*(-\mathbf{k})\end{bmatrix}, \tag{A2}$$

where the matrices $\mathcal{A}(\mathbf{k})$ and $\mathcal{B}(\mathbf{k})$ are

$$\mathcal{A}(\mathbf{k}) = \begin{bmatrix}1+\mathcal{D}_{\mathbf{k}} & -s_\theta f_{\mathbf{k}}\\ -s_\theta f^*_{\mathbf{k}} & 1-\mathcal{D}_{\mathbf{k}}\end{bmatrix},$$
$$\mathcal{B}(\mathbf{k}) = \begin{bmatrix}0 & (1-s_\theta)f_{\mathbf{k}}\\ (1-s_\theta)f^*_{\mathbf{k}} & 0\end{bmatrix}. \tag{A3}$$

$\mathcal{H}(\mathbf{k})$ is diagonalized by a paraunitary Bogoliubov transformation $\mathcal{U}_{\mathbf{k}}$ which satisfies $\Lambda\mathcal{H}_{\mathbf{k}}\mathcal{U}_{\mathbf{k}} = \mathcal{U}_{\mathbf{k}}\mathbf{E}_{\mathbf{k}}$ and $\mathcal{U}^\dagger_{\mathbf{k}}\Lambda\mathcal{U}_{\mathbf{k}} = \Lambda$, with $\mathbf{E}_{\mathbf{k}} = \mathrm{diag}(E_{+,\mathbf{k}}, E_{-,\mathbf{k}}, -E_{+,-\mathbf{k}}, -E_{-,-\mathbf{k}})$. According to the diagonalization procedure of the field operator transformation, we can write down directly the paraunitary transformation as

$$\mathcal{U}_{\mathbf{k}} = (|\Psi_+(\mathbf{k})\rangle \quad |\Psi_-(\mathbf{k})\rangle \quad |\bar{\Psi}_+(\mathbf{k})\rangle \quad |\bar{\Psi}_-(\mathbf{k})\rangle), \tag{A4}$$

where

$$|\Psi_+(\mathbf{k})\rangle = \begin{bmatrix}\cosh\chi_1\cos\psi\exp(i\varphi/2)\\ -\cosh\chi_1\sin\psi\exp(-i\varphi/2)\\ \sinh\chi_1\sin\psi\exp(i\varphi/2)\\ -\sinh\chi_1\cos\psi\exp(-i\varphi/2)\end{bmatrix},$$
$$|\Psi_-(\mathbf{k})\rangle = \begin{bmatrix}\cosh\chi_2\sin\psi\exp(i\varphi/2)\\ \cosh\chi_2\cos\psi\exp(-i\varphi/2)\\ \sinh\chi_2\cos\psi\exp(i\varphi/2)\\ \sinh\chi_2\sin\psi\exp(-i\varphi/2)\end{bmatrix}, \tag{A5}$$

and $|\bar{\Psi}_\pm(\mathbf{k})\rangle = C\Sigma_x|\Psi_\pm(-\mathbf{k})\rangle$. Here, C is the conjugate operator and

$$\Sigma_x = \begin{bmatrix}0 & I_{2\times2}\\ I_{2\times2} & 0\end{bmatrix}, \tag{A6}$$

where $I_{2\times2}$ is a two-by-two diagonal matrix. Note that $\chi_{1,2}$, ψ, and φ are all real functions of $\mathbf{k}$. We have omitted the $\mathbf{k}$ index for brevity. Specifically, we have

$$\cosh\chi_{1\mathbf{k}} = u_{1\mathbf{k}} = \sqrt{\frac{\mathcal{E}_{+,\mathbf{k}} + E_{+,\mathbf{k}}}{2E_{+,\mathbf{k}}}},$$
$$\sinh\chi_{1\mathbf{k}} = v_{1\mathbf{k}} = \sqrt{\frac{\mathcal{E}_{+,\mathbf{k}} - E_{+,\mathbf{k}}}{2E_{+,\mathbf{k}}}},$$
$$\cosh\chi_{2\mathbf{k}} = u_{2\mathbf{k}} = \sqrt{\frac{\mathcal{E}_{-,\mathbf{k}} + E_{-,\mathbf{k}}}{2E_{-,\mathbf{k}}}},$$
$$\sinh\chi_{2\mathbf{k}} = v_{2\mathbf{k}} = -\sqrt{\frac{\mathcal{E}_{-,\mathbf{k}} - E_{-,\mathbf{k}}}{2E_{-,\mathbf{k}}}}, \tag{A7}$$

with $\cos\psi_{\mathbf{k}} = \sqrt{(\eta_{\mathbf{k}} + \mathcal{D}_{\mathbf{k}})/2\eta_{\mathbf{k}}}$, $\sin\psi_{\mathbf{k}} = \sqrt{(\eta_{\mathbf{k}} - \mathcal{D}_{\mathbf{k}})/2\eta_{\mathbf{k}}}$, and $\varphi_{\mathbf{k}} = (1/i)\ln(f_{\mathbf{k}}/|f_{\mathbf{k}}|)$ which are also given in the main text.

APPENDIX B: THE TRANSFORMATIONS OF CUBIC HAMILTONIAN $H^{(3)}$

We write $H^{(3)}$ as

$$H^{(3)} = \sum_{\mathbf{k},\mathbf{q}}\sum_{\alpha\beta}\left(V^{\alpha\beta}_{\mathbf{q}} a^\dagger_{\beta\mathbf{q}} a^\dagger_{\alpha\mathbf{k}} a_{\alpha\,\mathbf{k}-\mathbf{p}} + \mathrm{H.c.}\right), \tag{B1}$$

where $-\mathbf{p} = \mathbf{k} + \mathbf{q}$ and the interacting vertices are given by the elements of the vertex matrix $V_{\mathbf{q}}$ as

$$V_{\mathbf{q}} = 3\sqrt{\frac{S}{2N}}\begin{bmatrix} -D\cos\theta g_{\mathbf{q}} & J\sin(2\theta) f^*_{\mathbf{q}} \\ J\sin(2\theta) f_{\mathbf{q}} & D\cos\theta g_{\mathbf{q}} \end{bmatrix}. \tag{B2}$$

For convenience, we define the following matrix:

$$W_{\mathbf{q}} = 3\sqrt{\frac{S}{2N}}\begin{bmatrix} -D\cos\theta g_{\mathbf{q}} & J\sin(2\theta)|f_{\mathbf{q}}| \\ J\sin(2\theta)|f_{\mathbf{q}}| & D\cos\theta g_{\mathbf{q}} \end{bmatrix}. \tag{B3}$$

Using an unitary transformation

$$a^\dagger_{\alpha\mathbf{k}} = e^{i(-1)^\alpha\varphi_{\mathbf{k}}/2}\sum_{\mu} T^{\alpha\mu}_{\mathbf{k}} c^\dagger_{\mu\mathbf{k}},$$

Eq. (B1) is written as

$$H^{(3)} = \sum_{\mathbf{k},\mathbf{q}}\sum_{\rho\nu\mu}\left(U^{\rho\nu\mu}_{\mathbf{qkp}} c^\dagger_{\rho\mathbf{q}} c^\dagger_{\nu\mathbf{k}} c_{\mu,-\mathbf{p}} + \text{H.c.}\right), \tag{B4}$$

where

$$U^{\rho\nu\mu}_{\mathbf{qkp}} = \sum_{\alpha\beta} W^{\alpha\beta}_{\mathbf{q}} T^{\beta\rho}_{\mathbf{q}} T^{\alpha\nu}_{\mathbf{k}} T^{\alpha\mu}_{-\mathbf{p}} \exp[(-1)^\alpha\tilde{\varphi}_{\mathbf{qkp}}], \tag{B5}$$

with $\tilde{\varphi}_{\mathbf{qkp}} = (\varphi_{\mathbf{q}} + \varphi_{\mathbf{k}} + \varphi_{\mathbf{p}})/2$ and $-\mathbf{p} = \mathbf{k} + \mathbf{q}$.

By denoting $M^{\alpha\beta,\rho\nu\mu}_{\mathbf{qkp}} = W^{\alpha\beta}_{\mathbf{q}} T^{\beta\rho}_{\mathbf{q}} T^{\alpha\nu}_{\mathbf{k}} T^{\alpha\mu}_{-\mathbf{p}}$ and defining

$$\begin{aligned} \bar{\mathcal{O}}^{\alpha\beta,\rho\nu\mu}_{\mathbf{qkp}} &= \frac{M^{\alpha\beta,\rho\nu\mu}_{\mathbf{qkp}} + M^{\alpha\beta,\rho\nu\mu}_{-(\mathbf{qkp})}}{2}, \\ \bar{\mathcal{A}}^{\alpha\beta,\rho\nu\mu}_{\mathbf{qkp}} &= \frac{M^{\alpha\beta,\rho\nu\mu}_{\mathbf{qkp}} - M^{\alpha\beta,\rho\nu\mu}_{-(\mathbf{qkp})}}{2}, \end{aligned} \tag{B6}$$

we can decompose $U^{\rho\nu\mu}_{\mathbf{qkp}}$ into $U^{\rho\nu\mu}_{\mathbf{qkp}} = \mathcal{O}^{\rho\nu\mu}_{\mathbf{qkp}} + \mathcal{A}^{\rho\nu\mu}_{\mathbf{qkp}}$. where

$$\begin{aligned} \mathcal{O}^{\rho\nu\mu}_{\mathbf{qkp}} &= \sum_{\alpha\beta}\bar{\mathcal{O}}^{\alpha\beta,\rho\nu\mu}_{\mathbf{qkp}}\exp[i(-1)^\alpha\tilde{\varphi}_{\mathbf{qkp}}], \\ \mathcal{A}^{\rho\nu\mu}_{\mathbf{qkp}} &= \sum_{\alpha\beta}\bar{\mathcal{A}}^{\alpha\beta,\rho\nu\mu}_{\mathbf{qkp}}\exp[i(-1)^\alpha\tilde{\varphi}_{\mathbf{qkp}}]. \end{aligned} \tag{B7}$$

It can be verified that, under the time reversal operation, $\mathcal{O}^{\rho\nu\mu}_{\mathbf{qkp}}$ is symmetric and $\mathcal{A}^{\rho\nu\mu}_{\mathbf{qkp}}$ is antisymmetric, i.e., $\mathcal{O}^{\rho\nu\mu}_{-(\mathbf{qkp})} = (\mathcal{O}^{\rho\nu\mu}_{\mathbf{qkp}})^*$ and $\mathcal{A}^{\rho\nu\mu}_{-(\mathbf{qkp})} = -(\mathcal{A}^{\rho\nu\mu}_{\mathbf{qkp}})^*$.

With the above definition and the transformation $c_{\mu\mathbf{k}} = u_{\mu\mathbf{k}} b_{\mu\mathbf{k}} + v_{\mu\mathbf{k}} b^\dagger_{\mu-\mathbf{k}}$, $H^{(3)}$ can be written in terms of $(b, b^\dagger)$ as

$$\begin{aligned} H^{(3)} = \sum_{\mathbf{k},\mathbf{q}}\sum_{\rho\nu\mu}\bigg(&\frac{1}{2!}\Gamma^{\rho\nu\mu}_{1,\mathbf{qkp}} b^\dagger_{\rho\mathbf{q}} b^\dagger_{\nu\mathbf{k}} b_{\mu-\mathbf{p}} \\ &+ \frac{1}{3!}\Gamma^{\rho\nu\mu}_{2,\mathbf{qkp}} b^\dagger_{\rho\mathbf{q}} b^\dagger_{\nu\mathbf{k}} b^\dagger_{\mu\mathbf{p}} + \text{H.c.}\bigg). \end{aligned} \tag{B8}$$

Here, the decay $\Gamma^{\rho\nu\mu}_{1,\mathbf{qkp}}$ and source $\Gamma^{\rho\nu\mu}_{2,\mathbf{qkp}}$ vertices are given as

$$\begin{aligned} \Gamma^{\rho\nu\mu}_{1,\mathbf{qkp}} &= \Gamma^{\rho\nu\mu}_{1S,\mathbf{qkp}} + \Gamma^{\rho\nu\mu}_{1A,\mathbf{qkp}}, \\ \Gamma^{\rho\nu\mu}_{2,\mathbf{qkp}} &= \Gamma^{\rho\nu\mu}_{2S,\mathbf{qkp}} + \Gamma^{\rho\nu\mu}_{2A,\mathbf{qkp}}, \end{aligned} \tag{B9}$$

where

$$\begin{aligned} \Gamma^{\rho\nu\mu}_{1S,\mathbf{qkp}} = {} & \mathcal{O}^{\rho\nu\mu}_{\mathbf{qkp}}(u_{\rho\mathbf{q}} + v_{\rho\mathbf{q}})(u_{\nu\mathbf{k}}u_{\mu\mathbf{p}} + v_{\nu\mathbf{k}}v_{\mu\mathbf{p}}) \\ & + \mathcal{O}^{\mu\nu\rho}_{\mathbf{pkq}}(u_{\mu\mathbf{p}} + v_{\mu\mathbf{p}})(u_{\nu\mathbf{k}}v_{\rho\mathbf{q}} + v_{\nu\mathbf{k}}u_{\rho\mathbf{q}}) \\ & + \mathcal{O}^{\nu\rho\mu}_{\mathbf{kqp}}(u_{\nu\mathbf{k}} + v_{\nu\mathbf{k}})(u_{\rho\mathbf{q}}u_{\mu\mathbf{p}} + v_{\rho\mathbf{q}}v_{\mu\mathbf{p}}), \\ \Gamma^{\rho\nu\mu}_{1A,\mathbf{qkp}} = {} & \mathcal{A}^{\rho\nu\mu}_{\mathbf{qkp}}(u_{\rho\mathbf{q}} - v_{\rho\mathbf{q}})(u_{\nu\mathbf{k}}u_{\mu\mathbf{p}} + v_{\nu\mathbf{k}}v_{\mu\mathbf{p}}) \\ & + \mathcal{A}^{\mu\nu\rho}_{\mathbf{pkq}}(v_{\mu\mathbf{p}} - u_{\mu\mathbf{p}})(u_{\nu\mathbf{k}}v_{\rho\mathbf{q}} + v_{\nu\mathbf{k}}u_{\rho\mathbf{q}}) \\ & + \mathcal{A}^{\nu\rho\mu}_{\mathbf{kqp}}(u_{\nu\mathbf{k}} - v_{\nu\mathbf{k}})(u_{\rho\mathbf{q}}u_{\mu\mathbf{p}} + v_{\rho\mathbf{q}}v_{\mu\mathbf{p}}), \end{aligned} \tag{B10}$$

and

$$\begin{aligned} \Gamma^{\rho\nu\mu}_{2S,\mathbf{qkp}} = {} & \mathcal{O}^{\rho\nu\mu}_{\mathbf{qkp}}(u_{\rho\mathbf{q}} + v_{\rho\mathbf{q}})(u_{\nu\mathbf{k}}v_{\mu\mathbf{p}} + v_{\nu\mathbf{k}}u_{\mu\mathbf{p}}) \\ & + \mathcal{O}^{\nu\mu\rho}_{\mathbf{kpq}}(u_{\nu\mathbf{k}} + v_{\nu\mathbf{k}})(u_{\mu\mathbf{p}}v_{\rho\mathbf{q}} + v_{\mu\mathbf{p}}u_{\rho\mathbf{q}}) \\ & + \mathcal{O}_{\mathbf{pqk}}(u_{\mu\mathbf{p}} + v_{\mu\mathbf{p}})(u_{\rho\mathbf{q}}v_{\nu\mathbf{k}} + v_{\rho\mathbf{q}}u_{\nu\mathbf{k}}), \\ \Gamma^{\rho\nu\mu}_{2A,\mathbf{qkp}} = {} & \mathcal{A}^{\rho\nu\mu}_{\mathbf{qkp}}(u_{\rho\mathbf{q}} - v_{\rho\mathbf{q}})(u_{\nu\mathbf{k}}v_{\mu\mathbf{p}} + v_{\nu\mathbf{k}}u_{\mu\mathbf{p}}) \\ & + \mathcal{A}^{\nu\mu\rho}_{\mathbf{kpq}}(u_{\nu\mathbf{k}} - v_{\nu\mathbf{k}})(u_{\mu\mathbf{p}}v_{\rho\mathbf{q}} + v_{\mu\mathbf{p}}u_{\rho\mathbf{q}}) \\ & + \mathcal{A}_{\mathbf{pqk}}(u_{\mu\mathbf{p}} - v_{\mu\mathbf{p}})(u_{\rho\mathbf{q}}v_{\nu\mathbf{k}} + v_{\rho\mathbf{q}}u_{\nu\mathbf{k}}). \end{aligned} \tag{B11}$$

It is noted that $\Gamma^{\rho\nu\mu}_{1S,\mathbf{qkp}}$ and $\Gamma^{\rho\nu\mu}_{2S,\mathbf{qkp}}$ retaining the time-reversal symmetry have the same form as the results obtained by Maksimov *et al.* [53], while $\Gamma^{\rho\nu\mu}_{1A,\mathbf{qkp}}$ and $\Gamma^{\rho\nu\mu}_{2A,\mathbf{qkp}}$ conserving the time-reversal antisymmetry originate from the DMI. As far as we know, this type of interacting vertices has not been studied so far.

---

[1] F. D. M. Haldane, Phys. Rev. Lett. **61**, 2015 (1988).

[2] C. L. Kane and E. J. Mele, Phys. Rev. Lett. **95**, 226801 (2005).

[3] S. A. Owerre, Phys. Rev. B **94**, 094405 (2016).

[4] S. A. Owerre, J. Phys.: Condens. Matter **28**, 386001 (2016).

[5] S. A. Owerre, J. Appl. Phys. **120**, 043903 (2016).

[6] S. S. Pershoguba, S. Banerjee, J. C. Lashley, J. Park, H. Ågren, G. Aeppli, and A. V. Balatsky, Phys. Rev. X **8**, 011010 (2018).

[7] Y.-S. Lu, J.-L. Li, and C.-T. Wu, Phys. Rev. Lett. **127**, 217202 (2021).

[8] A. Mook, K. Plekhanov, J. Klinovaja, and D. Loss, Phys. Rev. X **11**, 021061 (2021).

[9] T. Wehling, A. Black-Schaffer, and A. Balatsky, Adv. Phys. **63**, 1 (2014).

[10] J. Fransson, A. M. Black-Schaffer, and A. V. Balatsky, Phys. Rev. B **94**, 075401 (2016).

[11] R. Cheng, S. Okamoto, and D. Xiao, Phys. Rev. Lett. **117**, 217202 (2016).

[12] V. A. Zyuzin and A. A. Kovalev, Phys. Rev. Lett. **117**, 217203 (2016).

[13] Y. Su and X. R. Wang, Phys. Rev. B **96**, 104437 (2017).

[14] Z.-X. Li, Y. Cao, and P. Yan, Phys. Rep. **915**, 1 (2021).

[15] R. Hidalgo-Sacoto, R. I. Gonzalez, E. E. Vogel, S. Allende, J. D. Mella, C. Cardenas, R. E. Troncoso, and F. Munoz, Phys. Rev. B **101**, 205425 (2020).

[16] X. Zhai and Y. M. Blanter, Phys. Rev. B **102**, 075407 (2020).

[17] D. Ghader, Sci. Rep. **10**, 16733 (2020).

[18] D. Ghader, New J. Phys. **23**, 053022 (2021).

[19] Q.-H. Chen, F.-J. Huang, and Y.-P. Fu, Phys. Rev. B **105**, 224401 (2022).

[20] D. Xiao, W. Yao, and Q. Niu, Phys. Rev. Lett. **99**, 236809 (2007).

[21] V. Renard, B. Piot, X. Waintal *et al.*, Nat. Commun. **6**, 7230 (2015).

[22] D. Xiao, G.-B. Liu, W. Feng, X. Xu, and W. Yao, Phys. Rev. Lett. **108**, 196802 (2012).

[23] Z. Yu, H. Pan, and Y. Yao, Phys. Rev. B **92**, 155419 (2015).

[24] T. Habe and M. Koshino, Phys. Rev. B **96**, 085411 (2017).

[25] W. B. Yelon and R. Silberglitt, Phys. Rev. B **4**, 2280 (1971).

[26] E. J. Samuelsen, R. Silberglitt, G. Shirane, and J. P. Remeika, Phys. Rev. B **3**, 157 (1971).

[27] A. Wiedenmann, J. Rossat-Mignod, A. Louisy, R. Brec, and J. Rouxel, Solid State Commun. **40**, 1067 (1981).

[28] K. Okuda, K. Kurosawa, S. Saito, M. Honda, Z. Yu, and M. Date, J. Phys. Soc. Jpn. **55**, 4456 (1986).

[29] A. R. Wildes, K. C. Rule, R. I. Bewley, M. Enderle, and T. J. Hicks, J. Phys.: Condens. Matter **24**, 416004 (2012).

[30] D. Lançon, H. C. Walker, E. Ressouche, B. Ouladdiaf, K. C. Rule, G. J. McIntyre, T. J. Hicks, H. M. Rønnow, and A. R. Wildes, Phys. Rev. B **94**, 214407 (2016).

[31] G. Gitgeatpong, Y. Zhao, M. Avdeev, R. O. Piltz, T. J. Sato, and K. Matan, Phys. Rev. B **92**, 024423 (2015).

[32] G. Gitgeatpong, M. Suewattana, S. Zhang, A. Miyake, M. Tokunaga, P. Chanlert, N. Kurita, H. Tanaka, T. J. Sato, Y. Zhao *et al.*, Phys. Rev. B **95**, 245119 (2017).

[33] G. Gitgeatpong, Y. Zhao, P. Piyawongwatthana, Y. Qiu, L. W. Harriger, N. P. Butch, T. J. Sato, and K. Matan, Phys. Rev. Lett. **119**, 047201 (2017).

[34] L. Chen, J.-H. Chung, B. Gao, T. Chen, M. B. Stone, A. I. Kolesnikov, Q. Huang, and P. Dai, Phys. Rev. X **8**, 041028 (2018).

[35] B. Yuan, I. Khait, G.-J. Shu, F. C. Chou, M. B. Stone, J. P. Clancy, A. Paramekanti, and Y.-J. Kim, Phys. Rev. X **10**, 011062 (2020).

[36] K. Wang, X. Xu, Y. Cheng, M. Zhang, J.-S. Wang, H. Wang, and G. Zhang, Phys. Rev. B **102**, 235434 (2020).

[37] H. Katsura, N. Nagaosa, and P. A. Lee, Phys. Rev. Lett. **104**, 066403 (2010).

[38] P. Laurell and G. A. Fiete, Phys. Rev. B **98**, 094419 (2018).

[39] K.-S. Kim, K. H. Lee, S. B. Chung, and J.-G. Park, Phys. Rev. B **100**, 064412 (2019).

[40] R. Matsumoto, R. Shindou, and S. Murakami, Phys. Rev. B **89**, 054420 (2014).

[41] A. Mook, J. Henk, and I. Mertig, Phys. Rev. B **99**, 014427 (2019).

[42] A. Mook, J. Henk, and I. Mertig, Phys. Rev. B **89**, 134409 (2014).

[43] V. Bonbien, F. Zhuo, A. Salimath, O. Ly, A. Abbout, and A. Manchon, J. Phys. D **55**, 103002 (2022).

[44] Y. Onose, T. Ideue, H. Katsura, Y. Shiomi, N. Nagaosa, and Y. Tokura, Science **329**, 297 (2010).

[45] T. Ideue, Y. Onose, H. Katsura, Y. Shiomi, S. Ishiwata, N. Nagaosa, and Y. Tokura, Phys. Rev. B **85**, 134411 (2012).

[46] R. Chisnell, J. S. Helton, D. E. Freedman, D. K. Singh, R. I. Bewley, D. G. Nocera, and Y. S. Lee, Phys. Rev. Lett. **115**, 147201 (2015).

[47] M. Hirschberger, R. Chisnell, Y. S. Lee, and N. P. Ong, Phys. Rev. Lett. **115**, 106603 (2015).

[48] L. Zhang, J. Ren, J.-S. Wang, and B. Li, Phys. Rev. B **87**, 144101 (2013).

[49] S. A. Owerre, Phys. Rev. B **95**, 014422 (2017).

[50] S. A. Owerre, J. Appl. Phys. **121**, 223904 (2017).

[51] A. L. Chernyshev and M. E. Zhitomirsky, Phys. Rev. B **79**, 144416 (2009).

[52] M. E. Zhitomirsky and A. L. Chernyshev, Rev. Mod. Phys. **85**, 219 (2013).

[53] P. A. Maksimov and A. L. Chernyshev, Phys. Rev. B **93**, 014418 (2016).

[54] A. L. Chernyshev and M. E. Zhitomirsky, Phys. Rev. Lett. **113**, 237202 (2014).

[55] A. L. Chernyshev, Phys. Rev. B **92**, 094409 (2015).

[56] P. A. Maksimov, M. E. Zhitomirsky, and A. L. Chernyshev, Phys. Rev. B **94**, 140407(R) (2016).

[57] M. Mourigal, W. T. Fuhrman, A. L. Chernyshev, and M. E. Zhitomirsky, Phys. Rev. B **88**, 094407 (2013).

[58] A. L. Chernyshev and P. A. Maksimov, Phys. Rev. Lett. **117**, 187203 (2016).

[59] G. Murthy, D. Arovas, and A. Auerbach, Phys. Rev. B **55**, 3104 (1997).

[60] S. Miyashita, J. Phys. Soc. Jpn. **55**, 3605 (1986).

[61] D. Xiao, M.-C. Chang, and Q. Niu, Rev. Mod. Phys. **82**, 1959 (2010).

[62] N. Sivadas, M. W. Daniels, R. H. Swendsen, S. Okamoto, and D. Xiao, Phys. Rev. B **91**, 235425 (2015).

[63] A. R. Wildes, B. Roessli, B. Lebech, and K. W. Godfrey, J. Phys.: Condens. Matter **10**, 6417 (1998).